ChemPubSoc Europe

DOI: 10.1002/cssc.201600705

CHEMSUSCHEM Full Papers

Solar-Driven H_2O_2 Generation From H_2O and O_2 Using Earth-Abundant Mixed-Metal Oxide@Carbon Nitride Photocatalysts

Ruirui Wang,[a] Kecheng Pan,[a] Dandan Han,[a] Jingjing Jiang,[b] Chengxiang Xiang,[b] Zhuangqun Huang,[b, c] Lu Zhang,[a, b] and Xu Xiang*[a]

Light-driven generation of H_2O_2 only from water and molecular oxygen could be an ideal pathway for clean production of solar fuels. In this work, a mixed metal oxide/graphitic-C_3N_4 (MMO@C_3N_4) composite was synthesized as a dual-functional photocatalyst for both water oxidation and oxygen reduction to generate H_2O_2. The MMO was derived from a NiFe-layered double hydroxide (LDH) precursor for obtaining a high dispersion of metal oxides on the surface of the C_3N_4 matrix. The C_3N_4 is in the graphitic phase and the main crystalline phase in MMO is cubic NiO. The XPS analyses revealed the doping of Fe^{3+} in the dominant NiO phase and the existence of surface defects in the C_3N_4 matrix. The formation and decomposition kinetics of H_2O_2 on the MMO@C_3N_4 and the control samples, including bare MMO, C_3N_4 matrix, Ni- or Fe-loaded C_3N_4 and a simple mixture of MMO and C_3N_4, were investigated. The MMO@C_3N_4 composite produced 63 μmol L^{-1} of H_2O_2 in 90 min in acidic solution (pH 3) and exhibited a significantly higher rate of production for H_2O_2 relative to the control samples. The positive shift of the valence band in the composite and the enhanced water oxidation catalysis by incorporating the MMO improved the light-induced hole collection relative to the bare C_3N_4 and resulted in the enhanced H_2O_2 formation. The positively shifted conduction band in the composite also improved the selectivity of the two-electron reduction of molecular oxygen to H_2O_2.

Introduction

Hydrogen peroxide (H_2O_2) is a prevailing chemical oxidant, widely used in a variety of industrial fields owing to its low cost and environmentally benign characteristics.[1] For fuel cells, H_2O_2 is a clean energy source because the exhausts are only water and oxygen. H_2O_2 is superior to hydrogen or other fuel gasses because of its convenient and safe storage and transportation in liquid form. In addition, a single-compartment configuration is possible for H_2O_2 based fuel cells, which is structurally simpler and scales better than the two-compartment H_2 based fuel cells.[2] Despite these advantages, the production of H_2O_2 usually involves organic substances, produces undesirable by-products, and is highly energy-demanding (e.g., the anthraquinone oxidation process).[3] Many alternative approaches have been proposed to address these issues, such as photocatalytic generation of H_2O_2, which has distinctive advantages because solar energy is utilized and converted to a chemical fuel in this process without pollutant and carbon emission.[4]

The key to establishing solar-to-fuel conversion as a viable alternative is to develop efficient, stable, and scalable photocatalysts that could operate at mild conditions. TiO_2 has been used as a photocatalyst for H_2O_2 production. However, it produced a very low yield (several micromoles in hours) owing to its wide band gap (> 3 eV), or transparency to most of the visible light spectrum, and poor charge separation characteristics caused by defects and surface states.[5] To improve the performance of low-cost TiO_2 catalysts, the incorporation of noble metals or surface modification has been reported.[6] For example, Shiraishi et al. prepared a bimetallic AuAg-loaded TiO_2 photocatalyst that facilitated the charge separation of the photogenerated carriers and the decomposition of H_2O_2 was suppressed owing to the weakened adsorption of H_2O_2 on the TiO_2 surface.[6a] Maurino et al. demonstrated that the modification with F^- ions could effectively increase the catalytic activity toward H_2O_2.[6e] Zhao and his colleagues reported that phosphate-modified TiO_2 decreased the aggregation and decomposition of H_2O_2 on the surface.[6f] In addition to TiO_2, a graphitic carbon nitride (g-C_3N_4) photocatalyst has also shown high selectivity toward H_2O_2 in the presence of organic proton donors.[7] Carbon nitride has been demonstrated to be a photocatalyst for oxygen reduction by photoexcited electrons or se-

[a] R. Wang, K. Pan, D. Han, Dr. L. Zhang, Prof. Dr. X. Xiang
State Key Laboratory of Chemical Resource Engineering
Beijing University of Chemical Technology
15 Beisanhuan Dong Lu
Beijing 100029 (P.R. China)
E-mail: xiangxu@mail.buct.edu.cn

[b] J. Jiang, Dr. C. Xiang, Dr. Z. Huang, Dr. L. Zhang
Joint Center for Artificial Photosynthesis
California Institute of Technology
Pasadena, California, 91125 (USA)

[c] Dr. Z. Huang
AFM Business Unit
Bruker Nano Surfaces
Santa Barbara, California, 93117 (USA)

Supporting Information for this article can be found under: http://dx.doi.org/10.1002/cssc.201600704.

lective oxidation of organic substances by surface-reaching holes.[8] Lately, new $C_3N_3S_3$ polymer-based materials have been developed as efficient photocatalysts.[9] Particularly, the $Cd_3(C_3N_3S_3)_2$ coordination polymer showed robust photocatalytic H_2O_2 production from a methanol/water solution.[9a]

Despite the recent advancements, it is still a great challenge to produce H_2O_2 efficiently at a large scale using solar energy and earth-abundant elements.[10] Sacrificial hole acceptors such as alcohols have often been used to reduce the probability of electron–hole recombination, and thus facilitate the targeted reaction of dioxygen reduction into H_2O_2.[10b–d] These systems were not sustainable and resulted in the loss of chemical energy, the introduction of side products, and an increase in cost owing to the use of chemicals other than water. An energetically and economically wiser strategy would be to direct the photogenerated holes to oxidize water.[11] For instance, Fukuzumi and co-workers reported sustainable production of H_2O_2 from H_2O and O_2 by using a combination of a water oxidation catalyst (WOC), a photosensitizer, and a Lewis acid (Sc^{3+} ions), without using any sacrificial species.[11b] Shiraishi and co-workers have also demonstrated the production of H_2O_2 using g-C_3N_4 photocatalyst incorporated with pyromellitic diimide (PDI) units.[10a]

In this work, an all-earth abundant, mixed-metal oxide/graphitic-C_3N_4 (MMO@C_3N_4) was synthesized as a dual-functional photocatalyst for both the water oxidation and the oxygen reduction reactions. The two catalytic reactions were well-coupled on the MMO@C_3N_4 composite. To ensure the high dispersion of metal oxides on C_3N_4, a NiFe-layered double hydroxide (LDH) was utilized as a precursor for preparing the MMO. This strategy allowed more efficient exposure of the catalytically active sites on the MMO relative to the conventional solid-state synthesis.[12] The H_2O_2 was photocatalytically produced only from water and dioxygen without any sacrificial carbon-containing organic substances such as alcohols. This work provides a promising way for clean and sustainable production of H_2O_2 owing to the facile carbon-free synthesis, inexpensive chemical sources, and extremely accessible feedstocks (H_2O and O_2).

Results and Discussion

The morphology of C_3N_4 and MMO@C_3N_4 were characterized by TEM and AFM. Figure 1 A shows a typical structure of the bare C_3N_4 matrix. In contrast, the MMO@C_3N_4 composite exhibited particulate features with an average size of approximately 5.5 nm (Figure 1 B). Figure 1 C shows the high-resolution TEM (HRTEM) image of the MMO@C_3N_4 composite, in which the d-spacing in the (111) plane of NiO was measured to be 0.236 nm (inset). Furthermore, the MMO consisted of Ni, Fe, and O and the elements of the matrix were carbon and nitrogen, as shown in the EDS mapping (Figure 1 D). The iron oxides were also confirmed to be highly dispersed in the NiO phase.

The surface topography was studied by AFM in PeakForce tapping mode.[13] At the micrometer scale, the C_3N_4 matrix in

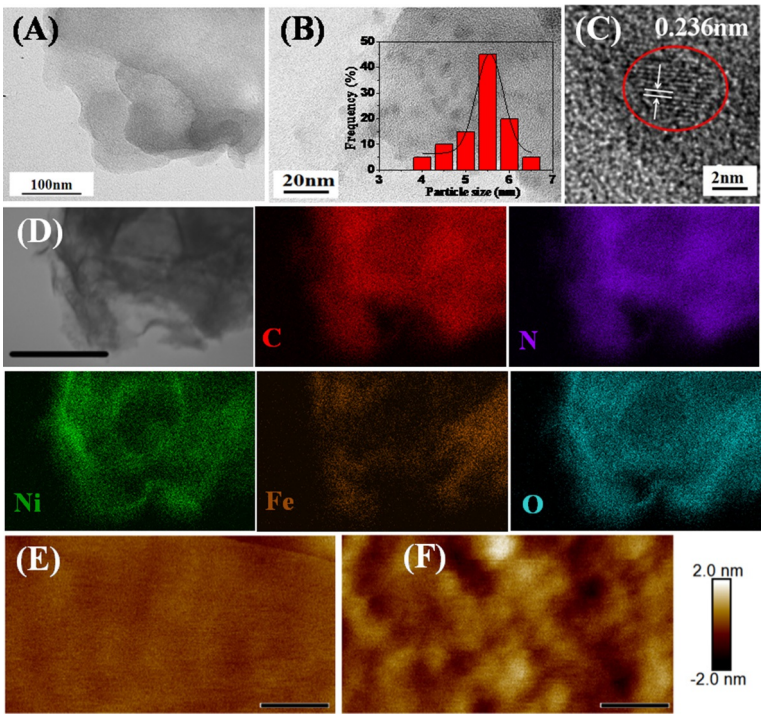

Figure 1. TEM images of (A) C_3N_4, (B) MMO@C_3N_4, and (C) HRTEM image of MMO@C_3N_4; the HRTEM lattice image in the inset of (C) shows a d-spacing of 0.236 nm, which is identified with the (111) plane of NiO. (D) EDS mapping of MMO@C_3N_4 (scale bar 500 nm). The elemental mappings showed the distribution of C, N, Ni, Fe, and O. The dark contrasts were oxide particles. The particles showed a Ni-rich feature. AFM images of (E) C_3N_4 and (F) MMO@C_3N_4 with a surface roughness of 0.199 and 0.438 nm, respectively. On the scale of $<$500 nm, (E) and (F) show the surface morphologies of the flat surface regions of these samples. The scale bars on the AFM images are 40 nm.

both the C_3N_4 and MMO@C_3N_4 samples showed hill and valley features with average heights of hundreds of nanometers (Figure S1A and S1B, Supporting Information). However, at the sub-micrometer scale, the C_3N_4 had a fairly smooth surface (Figure S1C), whereas the MMO@C_3N_4 composite had a much rougher surface and showed particulate features (Figure S1D). Figure 1E and 1F show detailed views of the C_3N_4 and MMO@C_3N_4 surfaces on a 200 nm range. The surface roughness of the C_3N_4 and MMO@C_3N_4 was 0.199 nm and 0.438 nm, respectively. The surface morphology obtained from the AFM measurements was consistent with the TEM observations, in which the MMO@C_3N_4 showed particles with an average size of approximately 5.5 nm dispersed onto the surface of the C_3N_4 matrix. The specific surface area of MMO@C_3N_4 was 18.6 $m^2 g^{-1}$, approximately 50% larger than the pristine C_3N_4 (12.6 $m^2 g^{-1}$). This could be ascribed to high dispersion of MMO on the C_3N_4 matrix.

Figure 2A–E shows the typical XRD patterns of C_3N_4, LDH@C_3N_4, MMO@C_3N_4, Ni@C_3N_4, and Fe@C_3N_4. All the reflection peaks were assigned to the graphitic carbon nitride (g-C_3N_4) with (100) and (002) lines, which come from in-plane repeating tri-s-triazine and stacking of the conjugated aromatic units, respectively.[14] No diffractions from the oxides or LDH were observed, indicating that they were highly dispersed into the C_3N_4 matrix. The formation of single phase LDH precursor was also verified by XRD (Figure 2F). The diffraction lines were indexed to a hydrotalcite-like structure (JCPDS 40-0215), which was consistent with the literature report.[15] The pattern of MMO derived from an LDH precursor was indexed to a cubic NiO phase (JCPDS 71-1179). No other crystalline phase was detected (Figure 2G). The molar ratio of Ni/Fe in MMO was measured by inductively coupled plasma atomic emission spectroscopy (ICP-AES) to be 2.8:1 (deviation $<10\%$), as expected from the nominal value (3:1) in the initial feedstock. The monometallic nickel and ferric samples after calcination were also analyzed to confirm the phase composition (Figure S2 and S3). To exclude the possibility that Ni and Fe directly coordinate with C_3N_4, FTIR measurements were conducted and compared. The FTIR spectrum of MMO@C_3N_4 exhibited the same absorption bands to that of C_3N_4 (Figure S4). No new bands appeared for MMO@C_3N_4. The results verified that the direct coordination of Ni and Fe with C_3N_4 is less likely.

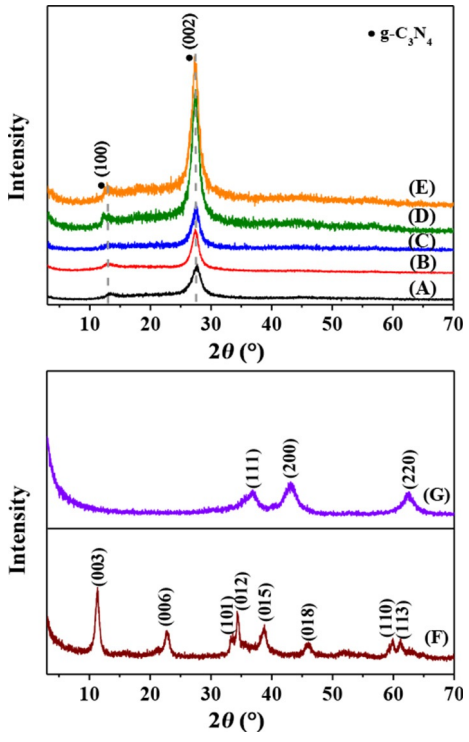

Figure 2. XRD patterns of the samples (A) C_3N_4, (B) LDH@C_3N_4, (C) MMO@C_3N_4, (D) Ni@C_3N_4, (E) Fe@C_3N_4, (F) LDH precursor, and (G) MMO.

The valence and binding information of the elements were determined by XPS. The core level spectra of Ni 2p in MMO@C_3N_4 were deconvoluted into two components in the Ni $2p_{3/2}$ region (Figure 3A). The component peak at 855.4 eV was higher than that of pure phase NiO (at ≈854.0 eV), partially because the high doping of Fe^{3+} with large electronegativity led to a higher valence state of Ni^{2+}.[16] The peak at 861.5 eV was assigned to the satellite of Ni^{2+} (sat.). The XPS analysis verified that the divalent NiO was a dominant species, and the Ni^{3+} was below the detection limit. For the Fe 2p spectra, three deconvoluted peaks appeared in the Fe $2p_{3/2}$ region (Figure 3B). The peak at 710.2 eV is characteristic of Fe^{2+}, and the neighboring one at 712.1 eV is the contribution of Fe^{3+}.[17] The co-existence of divalent and trivalent ferric species indicated that Fe^{2+}-containing species such as Fe_3O_4 could exist. The analyses of the N 1s spectra confirmed the existence of surface defects in the C_3N_4 matrix. Both N 1s spectra of the C_3N_4 and MMO@C_3N_4 samples were deconvoluted into three components (Figure 3C and D). For the C_3N_4 sample, the peaks at 398.9, 400.2, and 401.3 eV were assigned to sp^2-hybridized N atoms of the melem units ($N_{pyridine}$), trigonal N atoms of the melem center (N_{center}) and tertiary amine N atoms ($N_{tertiary}$) of the melem terminal, and the primary ($N_{primary}$) and secondary amine($N_{secondary}$) N atoms of the melem terminal, respectively.[18] The peak positions of these three components were within 0.1 eV of those in MMO@C_3N_4. However, the contribution of the component ($N_{primary}+N_{secondary}$) decreased in the N 1s spectra of MMO@C_3N_4. This was because the sites of the primary and secondary amine moieties were occupied by and coupled with the MMO particles. XPS is a surface-sensitive technique with a detection depth of several nanometers. The signal intensity of the specific sites on the surface decreases if these sites are partially occupied by foreign species.

The UV/Vis diffuse reflectance spectra of the composites and the controls are shown in Figure 4. The spectra were obtained by converting the reflection data measured using the Kubelka–Munk equation $F(R)=(1-R)^2/2R$, where R is the reflectance.[19] The C_3N_4 sample exhibited strong absorption below 420 nm, which was consistent with the previous reports.[8b] The MMO@C_3N_4 composite presented enhanced absorption below 400 nm relative to the C_3N_4. The Ni@C_3N_4 sample also exhibited stronger absorption in the UV wavelength region. In contrast, the mixture (MMO/C_3N_4-Mix) showed a small decrease in the absorption below 400 nm compared to the C_3N_4. This finding indicated that the improved absorption of MMO@C_3N_4 likely

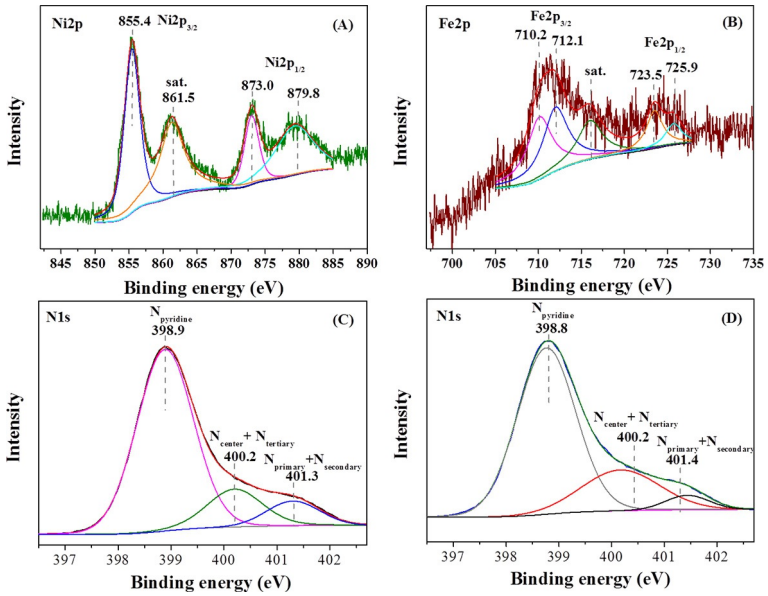

Figure 3. XPS core level spectra of (A) Ni 2p and (B) Fe 2p in MMO@C_3N_4, N 1s in (C) C_3N_4, and in (D) MMO@C_3N_4.

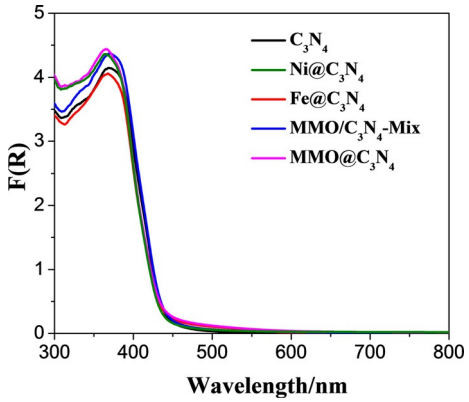

Figure 4. UV/Vis diffuse reflectance spectra of C_3N_4, MMO@C_3N_4, Ni@C_3N_4, Fe@C_3N_4, and MMO/C_3N_4-Mix.

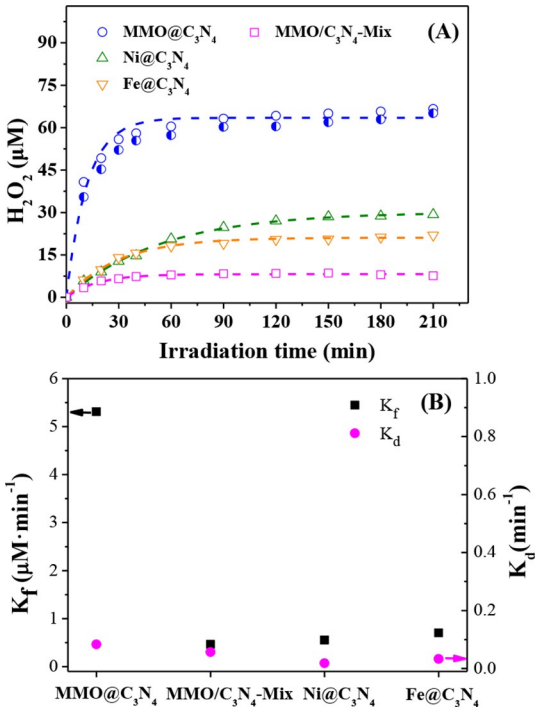

Figure 5. (A) The light-driven H_2O_2 generation in O_2-equilibrated conditions over MMO@C_3N_4, Ni@C_3N_4, Fe@C_3N_4, and MMO/C_3N_4-Mix; the semi-hollow circles (blue) represents the repeated use of the MMO@C_3N_4 photocatalyst. The experimental conditions were as follows: 1 g L^{-1} photocatalyst, pH 3, illumination intensity 100 mW cm^{-2}. (B) Formation rate constant (K_f) and decomposition rate constant (K_d) for H_2O_2 production.

originated from the strong interaction among the components rather than a simple physical mixing effect.[20]

The formations of H_2O_2 on various photocatalysts were conducted and monitored in an O_2-equilibrated acidic aqueous solution (pH 3) under irradiation with a Xe lamp at 100 mW cm^{-2}. As shown in Figure 5 A, the H_2O_2 was rapidly generated over the MMO@C_3N_4 photocatalyst within the first 30 min, with an initial rate that exceeded 4.0 μM min^{-1}. The concentration of the photogenerated H_2O_2 reached a plateau value of 63 μM after approximately 90 min. In the absence of photons and O_2 in the system, no H_2O_2 generation was observed (Figure S5 and S6). The content of MMO present in the MMO@C_3N_4 was optimized; the use of more or less MMO led to decreased H_2O_2 productivity (Figure S7). Table 1 shows the sustainable production of H_2O_2 from water and oxygen without any sacrificial hole acceptors. The photocatalytic activity of the MMO@C_3N_4 composite is among the best-reported photocatalysts to date. To elucidate the origin of the photocatalytic species, control experiments using the C_3N_4, MMO, Ni@C_3N_4, Fe@C_3N_4, and a mixture of MMO with C_3N_4 as the photocatalysts were also performed. First, both C_3N_4 and MMO samples produced undetectable H_2O_2 (< 0.01 μM after 210 min) under the same conditions. Second, as summarized in Table 1, the yield of H_2O_2 on

Table 1. Comparisons of H_2O_2 production on the as-prepared photocatalysts and the reported values in the literature.

Photocatalysts	Initial rate[a] [μM min^{-1}]	Rate constants K_f [μM min^{-1}]	K_d [min^{-1}]	K_d'[b] [min^{-1}]	H_2O_2 yield[c] [μM]
MMO@C_3N_4	4.0	5.3094	0.0836	0.0054	63
MMO/C_3N_4-Mix	0.33	0.4629	0.0566	–	8.3
Ni@C_3N_4	0.57	0.5542	0.0184	0.0032	24.7
Fe@C_3N_4	0.61	0.7019	0.0333	0.0021	19.0
g-C_3N_4/PDI[d]	–	–	–	–	31
rGO/TiO_2/CoPi[e]	–	–	–	–	66

[a] Initial rate was calculated using the yield of H_2O_2 after the first 10 min. [b] Initial H_2O_2 concentration: C_0 = 5 mM. [c] Yield at 90 min. [d] Data from Ref. [10a]. [e] Data from Ref. [11a].

the MMO@C_3N_4 composite after 90 min was 3.3 times higher than Fe@C_3N_4, 2.5 times higher than Ni@C_3N_4, and 7.6 times higher than the mixture MMO/C_3N_4-Mix with the same MMO loading on C_3N_4. These control experiments provided two important pieces of evidence that the catalytic enhancement resulted from the chemical interaction between MMO and C_3N_4 in the MMO@C_3N_4 composite. First, the sum of the yields after 90 min from both Ni@C_3N_4 and Fe@C_3N_4 were 43.7 μM. The sum of the yields was still 31% lower than that of the composite. Second, the simple mixture only resulted in the initial production rate of 0.33 μM min^{-1} and 12% yield (8.3 μM) after 90 min relative to the composite. These two pieces of evidence suggested that the strong interaction between MMO and C_3N_4 induced by in situ hydrothermal growth and subsequent calcination is favorable to endow the photocatalyst with excellent activity for H_2O_2 production.

The formation and decomposition of H_2O_2 on the photocatalysts proceeds through two competitive pathways owing to the thermodynamic instability of H_2O_2 at room temperature.[6e, 11a] To further understand the mechanism of H_2O_2 generation, a well-established kinetic model shown in Equation (1) was used to understand the behavior of the H_2O_2 concentration as a function of time.

$$[H_2O_2] = \frac{K_f}{K_d}(1 - e^{K_d t}) \quad (1)$$

In Equation (1), K_f and K_d are the formation and decomposition rate constants, respectively.[21] In this model, the formation rate follows zero-order kinetics owing to the continuous O_2 purge, whereas the decomposition rate follows first-order kinetics. The dashed lines in Figure 5A are the fitting results using Equation (1). According to the parameters fitted (Figure S8), K_f and K_d were compared in Table 1 and plotted in Figure 5B. The formation rate, i.e., K_f of MMO@C_3N_4 was approximately one order of magnitude larger than the other three control samples (5.3 vs. 0.4–0.7 μM min^{-1}). The MMO@C_3N_4 composite also exhibited a higher decomposition rate, approximately 1.5–4.5 times higher relative to the control samples. However, the decomposition rate of H_2O_2 even for this most active MMO@C_3N_4 composite was fairly slow, i.e., approximately 0.0836 min^{-1}. Consequently, the generation of H_2O_2 mostly depended on the K_f rather than K_d in the initial stage, during which the formation greatly outperformed the decomposition. This is inconsistent with the latest results observed for a reduced graphene oxide (rGO)/TiO_2 photocatalyst and its control samples, whereby the catalyst with the smallest K_d had the best overall production of H_2O_2.[11a]

To study the stability of the MMO@C_3N_4 photocatalyst, the used catalyst sample was separated from the solution after the reactions, washed, and dried. Subsequently, the photocatalyst was re-used in a fresh solution for monitoring the generation of H_2O_2 under the same conditions. As shown in Figure 5A (semi-hollow circles in blue), the performance of the recycled MMO@C_3N_4 photocatalyst exhibited marginal degradation (<5%) as compared to that of the fresh sample. The performance was almost unchanged even after it was recycled 5 times (Figure S9). The structural characterizations by IR, XRD, and HRTEM proved that the MMO@C_3N_4 was stable after it was used in catalytic reactions (Figure S10, S11, and S12). In addition, the elemental analyses by ICP indicated that the etching of Ni and Fe in the MMO@C_3N_4 was below 5% after the reactions. This high repeatability of photocatalytic activity is not only a strong evidence of the stability of the material but also has a great value for practical use.

Suppression of the decomposition of H_2O_2 is an efficient way to increase the yield of light-driven H_2O_2 production. The use of TiO_2 nanoparticles as a photocatalyst, for example, the surface modification of TiO_2 by F^- ions, enhances the activity toward H_2O_2 production.[6e] In this work, the decomposition behavior of H_2O_2 in the presence of photocatalysts was further investigated. The experiments were conducted in an acidic solution (pH 3) with an initial H_2O_2 concentration of 5 mM. The concentration of H_2O_2 decreased by <7% over C_3N_4 after 90 min illumination (Figure 6). In contrast, the H_2O_2 decomposed approximately 40% over MMO@C_3N_4 after 90 min, higher than those over the control Ni@C_3N_4 (25%) and Fe@C_3N_4 (19%). In the absence of any catalysts, the decomposition of H_2O_2 was less than 3% after 90 min illumination.

Owing to the large quantity of H_2O_2 (5 mM) and the constant amounts of the catalysts, the decomposition is expected to follow a pseudo-first-order reaction [Eq. (2)]:

$$-\frac{dC(t)}{dt} = k_0' \text{ or } C(t) = -k_0' t + C_0 \quad (2)$$

where $C(t)$ is the H_2O_2 concentration at time t, k_0' is the pseudo-first-order rate constant, and C_0 is the initial concentration of H_2O_2 (5 mM) in this work. To more accurately derive the rate constants, we fit these decomposition plots using a first-order reaction equation, where k_1 is the first-order reaction rate constant. The results indicated that the order of k_1 followed MMO@C_3N_4 (0.0054 min^{-1}) > Ni@C_3N_4 (0.0032 min^{-1}) > Fe@C_3N_4 (0.0021 min^{-1}) > C_3N_4(0.00075 min^{-1}) (Figure S13). Compared to the decomposition rate in the photocatalytic system, MMO@C_3N_4 remained the most active among all the catalysts, i.e., had the largest decomposition rate constant. Fur-

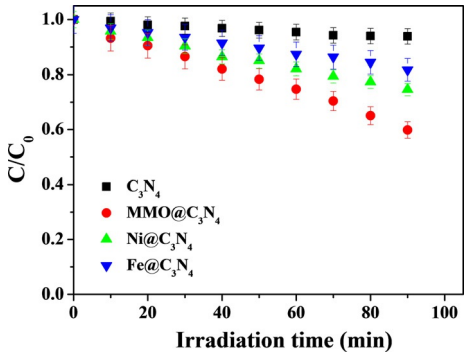

Figure 6. The photocatalytic decomposition of H_2O_2 ($C_0 = 5$ mM) over C_3N_4, MMO@C_3N_4, Ni@C_3N_4, and Fe@C_3N_4. The experimental conditions were as follows: 1 g L^{-1} photocatalyst, pH 3, illumination intensity 100 mW cm^{-2}.

thermore, all the rate constants were one order of magnitude lower than those for the photocatalytic reactions used for the generation of H_2O_2. This indicated that photons activated these catalysts to reduce kinetic barrier so that both the forward and backward reactions were accelerated. However, owing to the sluggish kinetics, the impact of illumination on the back reactions only played a trivial role in the total generation of H_2O_2.

The production of H_2O_2 also depended on the pH of the solution, as the generation of H_2O_2 is a proton-coupled electron transfer process.[11a,b] In this regard, we tested three different pH values (1, 3, and 5) in an aqueous solution of $HClO_4$ (Figure S14). At pH 5, the MMO@C_3N_4 only produced approximately 7 μM of H_2O_2 after 210 min, which was one order of magnitude lower than at pH 3 and pH 1. In the case of pH 3 and pH 1, the plots showed a similar formation rate up to approximately 30 min and subsequently separated from each other with yields of 66 μM at pH 3 and 88 μM at pH 1 after 210 min (Figure S14). This indicated that a higher pH results in faster H_2O_2 decomposition. In addition, to exclude the effect of urea hydrolysis on the H_2O_2 generation over C_3N_4, the control sample C_3N_4(urea) was prepared (see details in the Experimental Section). This control showed negligible activity toward H_2O_2 generation under the same operational conditions (Figure S15).

We have extensively characterized the MMO@C_3N_4 photocatalysts that were suspended into the solution for the generation of H_2O_2. All the spectroscopic and photocatalytic studies above indicated that the chemical interaction and structural optimization favored enhanced charge separation, facilitating the formation of H_2O_2. Furthermore, these studies also suggested that the MMO@C_3N_4 acted as a dual-functional catalyst for both water oxidation and O_2 reduction. To confirm this, we also performed the studies focused on the half reactions, i.e., water oxidation and oxygen reduction. We prepared catalyst-casted fluorine-doped tin oxide (FTO) electrodes and these electrodes were used in a three-electrode electrochemical cell. Such a setup has been used to evaluate transition metal oxides serving as WOCs.[16a,22] For example, in relation to this work, Fe-doped NiO or $NiFeO_x$ have been reported to be efficient WOCs.[23] Figure 7 A shows linear sweep voltammogram

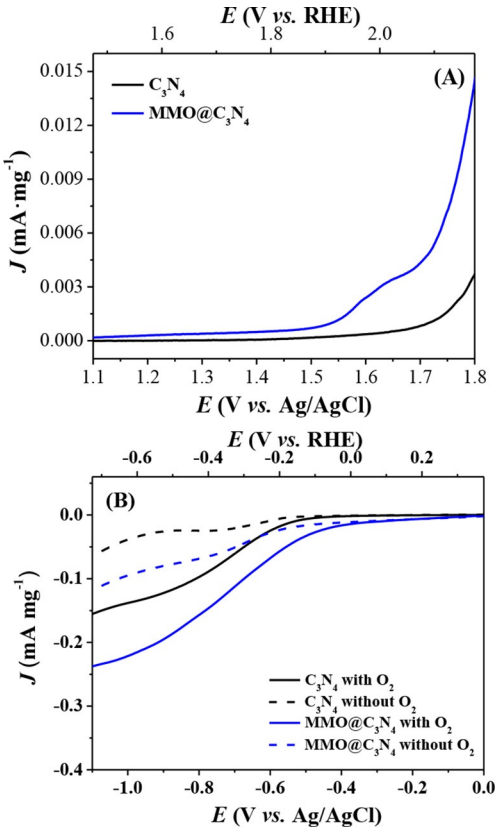

Figure 7. (A) Linear sweep voltammetry (LSV) curves of catalyst-loaded electrodes for C_3N_4 and MMO@C_3N_4 toward oxygen-evolving reaction, (B) LSV curves of catalyst-loaded electrodes for C_3N_4 and MMO@C_3N_4 under N_2- or O_2-equilibrated conditions, respectively. N_2-equilibrated conditions: Before reaction, the solution was purged with N_2 for 12 h. O_2-equilibrated conditions: continuous O_2 purge during the experiments. Acidic solution (pH 3), scan rate 10 mV s^{-1}.

(LSV) curves of the electrodes with the catalysts from this work. The catalysts were dispersed in Nafion solution and cast onto the FTO conductive glass as working electrodes. The onset potential of C_3N_4 for water oxidation was at approximately 2.1 V vs. reversible hydrogen electrode (RHE) in the dark, which had a 0.9 V overpotential because the thermodynamic potential was 1.23 V vs. RHE. In addition, the slow increase of the current density (J) with bias (E) indicated a high kinetic barrier. However, for the MMO@C_3N_4, the onset potential negatively shifted to approximately 200 mV, and the current density was greatly enhanced compared to the C_3N_4. For example, at 1.75 V (vs. Ag/AgCl), the current density of MMO@C_3N_4 had a 4.6 times increase (0.00723 vs. 0.00161 mA mg^{-1}). Also, MMO@C_3N_4 showed semiconductor/liquid junction characteristics featured by a leaky diode behavior of the J–E curve. In addition, the MMO@C_3N_4 was compared with the control LDH@C_3N_4 in oxygen-evolving reaction (OER). Although the LDH@C_3N_4 has a comparable OER performance to the MMO@C_3N_4 (Figure S16), the former is not applicable in the present acidic solution (pH 3) because of the alkaline feature of LDH. The LDH@C_3N_4 also showed inferior activity toward H_2O_2 generation (Figure S17).

We also investigated the catalytic activities of the FTO electrodes with MMO@C_3N_4 and the C_3N_4 control for O_2 reduction. As shown in Figure 7B, in the absence of O_2, C_3N_4 had a current density < -0.05 mA mg^{-1} at a bias of -1.0 V vs. Ag/AgCl, which was likely owing to proton reduction. Although MMO@C_3N_4 roughly doubled this value, it remained less than -0.1 mA mg^{-1} when the potential was more positive than -1.0 V vs. Ag/AgCl. In the continuous O_2 purge, these current density values were greatly improved, e.g., -0.138 mA mg^{-1} for C_3N_4 and -0.22 mA mg^{-1} for MMO@C_3N_4 at -1.0 V vs. Ag/AgCl. The persistent increase of the reduction current and the absence of a current plateau indicated a two-electron reduction of O_2 to HOO^-.[24] This 60% enhancement in current density of MMO@C_3N_4 relative to C_3N_4 confirmed that the composite was also a good oxygen reduction catalyst (ORC) in addition to a WOC. This proved that MMO@C_3N_4 served as both a WOC and an ORC, i.e., a dual-function catalyst in the case of a suspension solution. In addition, comparing Figure 7A,B, the current density of water oxidation was approximately one order of magnitude lower than that of O_2 reduction. This was expected as O_2 evolution is a proton-coupled four-electron process whereas O_2 reduction only requires two electrons.

The chronoamperometric traces of catalyst-loaded electrodes were further measured under chopped light to compare the photoresponsive behaviors. The C_3N_4 showed a steady-state photocurrent density of 0.11 mA g^{-1} for water oxidation upon light-on (Figure 8). In contrast, the MMO@C_3N_4 had a photocurrent density of 0.28 mA g^{-1}, which was 2.5 times higher than the bare C_3N_4. Furthermore, the photocurrent was stable and had little decay under illumination. As for the controls, Ni@C_3N_4 and Fe@C_3N_4 had a much lower photocurrent density (0.13–0.14 mA g^{-1}) than MMO@C_3N_4. This indicated that the MMO (Fe-doped NiO) exhibited higher water oxidation capability than the respective monometallic counterparts. As a consequence, the photoelectrochemical (PEC) measurements confirmed the superiority of MMO@C_3N_4 for water oxidation.

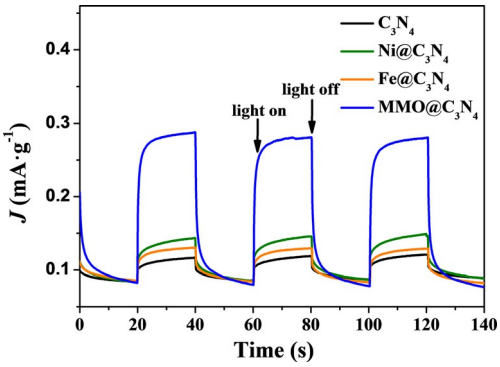

Figure 8. Current density–time traces of catalyst-loaded electrodes under chopped light in acidic solution (pH 3) for C_3N_4, MMO@C_3N_4, Ni@C_3N_4, and Fe@C_3N_4. The potential applied was 1.5 V vs. Ag/AgCl. Back illumination, intensity 100 mW cm^{-2}.

The activity and selectivity of the oxygen reduction reactions are highly dependent on the band edge positions of the semiconductor materials. The flat band potentials (E_{fb}) of C_3N_4 and MMO@C_3N_4 in contact with an electrolyte at pH 3 were estimated by electrochemical Mott–Schottky measurements at varied frequencies. The Mott–Schottky plots of both samples exhibited positive slopes, suggestive of their n-type semiconductor features (Figure 9).[25] The E_{fb} value was estimated by extrapolating the linear portion of the curve to intercept the *x*-axis.[26] A flat band potential of -0.71 V and -0.026 V vs. RHE was obtained for C_3N_4 and MMO@C_3N_4, respectively. The conduction band could be 0–0.1 V more negative than the flat band position. Hence, the corresponding conduction band edge of C_3N_4 and MMO@C_3N_4 was estimated to be -0.81 V and -0.126 V vs. RHE, respectively. A positive shift of 0.684 V from the bare C_3N_4 to the MMO@C_3N_4 composite was observed. The positive shift of the conduction band in the composite was likely to improve the selectivity of the oxygen reduction to H_2O_2.[10a]

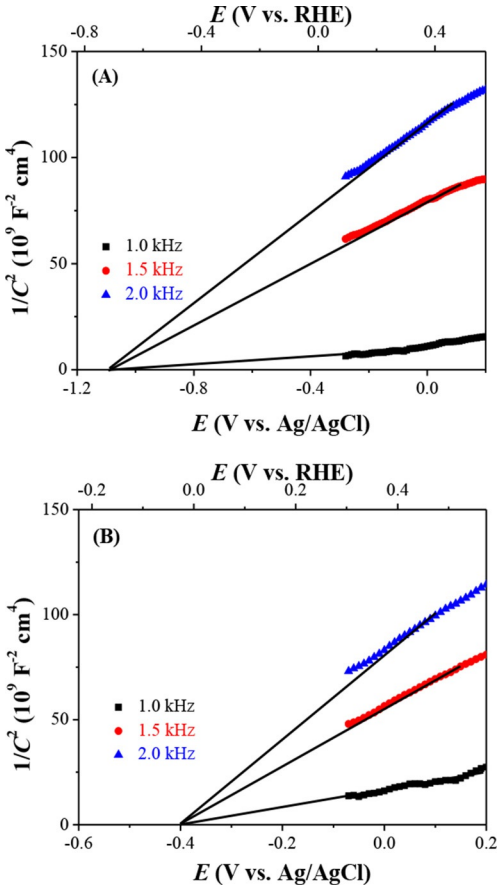

Figure 9. Mott–Schottky plots of (A) C_3N_4 and (B) MMO@C_3N_4 in acidic solution (pH 3) in the dark. The frequency used was 1.0 kHz, 1.5 kHz, and 2.0 kHz.

The Tauc plots of C_3N_4 and MMO@C_3N_4 were derived according to the relationship of $(F(R)\cdot h\upsilon)^2 = A(h\upsilon - E_g)$, where h is Plank's constant, υ is the frequency, A is a constant, and E_g is the material band gap (Figure S18).[19,27] From the Tauc plots, the MMO@C_3N_4 has a band gap of 2.89 eV, which is 0.01 eV larger than that of C_3N_4 (2.88 eV). The band gap value of C_3N_4

was close to that of bulk g-C_3N_4 reported in the literature.[28] The valence band (VB) positions were estimated according to the band gap and the conduction band (CB) positions. Both the CB and VB were more positive in MMO@C_3N_4 (Figure 10).

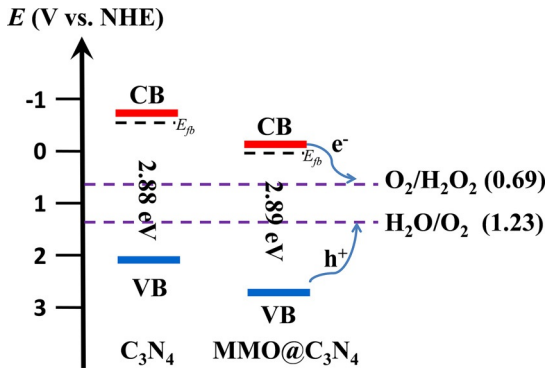

Figure 10. Scheme of energy levels and charge transfer pathways of C_3N_4 and MMO@C_3N_4. The positive shift of the valence band in the MMO@C_3N_4 promoted hole-involved water oxidation and the positive shift of the conduction band improved the selectivity of the oxygen reduction through a two-electron pathway. The potentials of O_2/H_2O_2 and H_2O/O_2 are also indicated.

Because the water oxidation is a rate-limiting step, the positive shift of the VB in MMO@C_3N_4 facilitated to overcome the kinetic barrier of the sluggish O_2 evolution. In addition, its CB level was 0.816 V more negative than the reduction potential of O_2/H_2O_2 (0.69 V vs. RHE).[29] This finding was very similar to that of g-C_3N_4/PDI, in which both the CB and VB levels of g-C_3N_4 were shifted positively with increasing PDI units.[10a] It was confirmed that the positive shifts of VB enhance the capability of g-C_3N_4 for water oxidation and provide sufficient potentials for O_2 reduction.

According to the results and the energy levels analyzed above, we proposed a tentative mechanism for H_2O_2 production over the MMO@C_3N_4 photocatalyst. The light irradiation on MMO@C_3N_4 led to enhanced charge separation owing to the reduced band gap and the presence of MMO as a WOC. The photogenerated holes were involved in the water oxidation promoted by the chemical incorporation of MMO owing to the positive shift of the valence band level. The separated electrons reduced dioxygen by a proton-coupled two-electron pathway to generate H_2O_2. The more positive potential of the valence band elevated the driving force to climb the large barrier for water oxidation, efficiently promoting photogenerated hole separation and involvement in surface oxidation reactions. Simultaneously, the sufficient potential difference (0.816 V) between the conduction band of MMO@C_3N_4 (−0.126 V vs. RHE) and O_2 reduction potential (0.69 V vs. RHE) guaranteed the occurrence of O_2 reduction reactions.

Conclusions

A dual-functional MMO@C_3N_4 composite photocatalyst was synthesized from an LDH@C_3N_4 precursor for light-driven generation of H_2O_2 in an acidic solution. The MMO particles consisting of Fe-doped NiO were chemically incorporated into the graphitic phase C_3N_4 matrix. The formation and decomposition kinetics studies of H_2O_2 indicated that the MMO@C_3N_4 composite possessed much higher productivity of H_2O_2 relative to the controls. The production of H_2O_2 also depended on the pH of the solution. Lower pH resulted in higher yield of H_2O_2. The enhanced productivity of H_2O_2 was ascribed to the improved capability toward water oxidation because the valence band of the MMO@C_3N_4 catalyst was positively shifted as compared to the bare C_3N_4. Both the cyclic voltammetry (CV) measurements in the dark and the photoelectrochemical current density–time (*J*–*t*) verified the superiority of MMO@C_3N_4 for water oxidation. Simultaneously, the positive shift of the conduction band in the composite improved the selectivity of the two-electron reduction of dioxygen toward the formation of H_2O_2. Tuning of the band edges was achieved by chemical coupling of MMO and C_3N_4 on the nanoscale, which could be an important pathway for the design of C_3N_4-based composites with improved oxygen reduction performance. This study dictates a promising way for clean and sustainable production of H_2O_2 using only water and oxygen over an earth-abundant catalyst.

Experimental Section

Materials

Melamine (1,3,5-triazine-2,4,6-triamine, $C_3H_6N_6$, 99%), $Ni(NO_3)_2{\cdot}6H_2O$ (nickel nitrate hexahydrate), $Fe(NO_3)_3{\cdot}9H_2O$ (iron nitrate nonahydrate), urea, H_2SO_4 (sulfuric acid), $HClO_4$ (perchloric acid), KH_2PO_4 (potassium dihydrogen phosphate), and $K_2HPO_4{\cdot}3H_2O$ (potassium hydrogen phosphate, trihydrate) were purchased from Sinopharm Chemical Reagent (Beijing Co. Ltd.). All reagents were of analytical grade and were used without further purification. Deionized water was used throughout the experiments.

Preparation of graphitic-Carbon Nitride (g-C_3N_4)

The g-C_3N_4 was prepared by directly heating of a melamine precursor, as described by Chen et al.[14] In a typical synthesis, melamine (3.0 g) was added to a porcelain cup and calcined at 520 °C for 4 h with a heating rate of 4 °C min^{-1}. Grinding of the product resulted in yellow powders.

Synthesis of LDH@C_3N_4 and MMO@C_3N_4 composites

The LDH@C_3N_4 precursor was synthesized by a hydrothermal method using urea as a precipitator. In a typical procedure, $Ni(NO_3)_2{\cdot}6H_2O$ (0.3 mmol), $Fe(NO_3)_3{\cdot}9H_2O$ (0.1 mmol), and urea (2 mmol) were dissolved in 50 mL of water and stirred to form a clear solution. The as-synthesized C_3N_4 powder was added to the solution and sonicated for 1 h. The molar ratio of C_3N_4 to the Fe^{3+} ions was 300:1. The suspension was transferred to a Teflon-lined stainless-steel autoclave and maintained at 120 °C for 12 h. The resultant suspension was filtered and washed with water until the pH of the filtrate reached 7. The wet products were dried at 70 °C in a vacuum oven overnight. The obtained LDH@C_3N_4 composites were calcined at 300 °C for 1 h in air (heating rate of 5 °C min^{-1}), during which LDH was transformed into MMO. The products were denoted as MMO@C_3N_4. To exclude the effect of urea hydrolysis on

the structure of C_3N_4, the as-synthesized C_3N_4 powder was subject to the same urea hydrolysis reaction (at 120 °C, 12 h) without the addition of metal ions feedstock. The product was calcined at 300 °C for 1 h. The sample was denoted as C_3N_4(urea). Single phase LDH was prepared using the same conditions with no addition of C_3N_4. In addition, MMO was produced by calcining the LDH precursor at 300 °C for 1 h in air.

For comparisons, monometallic nickel or ferric oxides and the corresponding composites with C_3N_4 were prepared by the same procedure only adding single metal salts during the synthesis. The molar ratio of C_3N_4 to the Ni^{2+} ions was 100:1 and C_3N_4 to the Fe^{3+} ions was 300:1, which was the same as the ratio in MMO@C_3N_4. The products were named Ni@C_3N_4 and Fe@C_3N_4. In addition, a mixture of MMO and C_3N_4 was prepared by a grinding-heating method. The C_3N_4 powder was mixed with LDH in an agate mortar. The mixture was calcined at 300 °C for 1 h in air. The product was named MMO/C_3N_4-Mix. The ratio of C_3N_4 to MMO was the same as that in MMO@C_3N_4.

Characterizations

HRTEM images were recorded using a JEOL JEM-3010 microscope. For TEM observations, the samples were ultrasonically dispersed in ethanol, and then a drop of the suspension was deposited onto a carbon-coated copper grid followed by evaporation of the solvent in air. Energy dispersive X-ray spectroscopy (EDS) mapping analysis was performed by using a JEOL JEM-2010F microscope combined with an EDX (OxFord X-Max^N 80-TLE) spectrometer. Surface topography imaging was conducted on a Bruker Dimension ICON AFM. The mode for surface mapping was PeakForce Quantitative Nano Mechanics. Bruker MPP-12120-10 probes were used. The normal mechanical specifications of the rectangular cantilever were a spring constant of 5 N/m and a resonance frequency 150 kHz. For AFM imaging, powder samples were cast onto FTO electrodes as described in the "Electrochemical tests" section below. The XRD patterns of the samples were collected on a Shimadzu XRD-6000 diffractometer (40 kV, 30 mA, graphite-filtered CuK_α radiation, $\lambda = 0.15418$ nm). Elemental analyses were performed using ICP-AES on a Shimadzu ICPS-7500 spectrometer. The XPS spectra were recorded on a ThermoVG ESCALAB MK II X-ray photoelectron spectrometer at a pressure of about 2×10^{-9} Pa by using AlK_α X-ray as the excitation source (1486.6 eV). The positions of all binding energies were calibrated by using the C 1s line at 284.8 eV. Solid-state UV/Vis absorption spectra were recorded at room temperature using a Shimadzu UV-3000 spectrometer equipped with an integrating sphere attachment using $BaSO_4$ as a background.

Photocatalytic production and decomposition of H_2O_2

The catalyst (1 g L^{-1}) was added to water (30 mL) within a borosilicate glass bottle ($\varphi = 35$ mm, capacity 50 mL) and was dispersed by ultrasonication for 10 min. The pH of the suspension was adjusted to pH 3 by adding $HClO_4$ solution (1 mol L^{-1}). The bottle was sealed with a rubber septum cap with a gas inlet and outlet. The solution was first purged by oxygen bubbling while stirring in dark for 30 min. The solution was illuminated using a 300 W Xenon lamp at 100 mW cm^{-2} under magnetic stirring. The oxygen purging was maintained throughout the reaction. The solution was sampled at certain times to determine the concentration of H_2O_2. After the first photocatalytic H_2O_2 formation run for 210 min, the MMO@C_3N_4 photocatalyst was removed by centrifugation and washed thoroughly with water and dried under a flow of N_2. Subsequently, the used MMO@C_3N_4 photocatalyst was reused in a fresh solution under the same conditions. To investigate the decomposition behavior of H_2O_2 over the photocatalysts, a sample of 1 g L^{-1} was dispersed in H_2O_2 solution (initial concentration: 5 mM, pH 3) and irradiated for 90 min under continuous stirring.

The concentration of hydrogen peroxide was determined according to the literature.[11] The stock solutions of *N*,*N*-diethyl-1,4-phenylene-diamine sulfate (DPD), peroxidase (POD) horseradish, and potassium phosphate buffer were prepared as follows. DPD (0.1 g) was dissolved in 10 mL of 0.1 N H_2SO_4 solution, and POD (5 mg) was dissolved in 5 mL of water. The POD solution was kept in a refrigerator (4 °C) and was prepared once every five days. $K_2HPO_4{\cdot}3H_2O$ (1.4 g) and KH_2PO_4 (6 g) were dissolved in 100 mL of water to make potassium phosphate buffer solution. Two milliliter aliquots were removed by a syringe during the irradiation at fixed times and filtered through a 0.45 μm polytetrafluoroethylene (PTFE) filter. Phosphate buffer (0.8 mL), 2 mL of the sample aliquots, DPD (0.1 mL), POD (0.1 mL), and 2.24 mL of water were mixed and stirred vigorously for 90 sec. Depending on the concentration of H_2O_2, the ratio of the sample aliquot/water was changed to avoid exceeding the detection limit of this method. The calibration curves of H_2O_2 concentration were made based on the range of the H_2O_2 concentration. The absorbance at 551 nm was measured using a UV/Vis spectrophotometer for quantitative analyses.

Electrochemical tests

The electrochemical water oxidation of the samples was studied using a three-electrode cell connected to a potentiostat (CHI660E, CH instrument Co. USA). The Ag/AgCl electrode and Pt wire were used as reference and counter electrode, respectively. The working electrode was fabricated by immobilizing samples on the FTO conductive glass by a casting method. The as-prepared samples (10 mg) were dispersed in a solution (ethanol: 800 μL, Nafion: 200 μL), and sonicated for 3 h. Subsequently, the resultant suspension was cast dropwise on the surface of the FTO. The FTO electrodes immobilized with the samples were connected to a copper tape and used as the working electrode. The LSV measurements were obtained in an aqueous solution of $HClO_4$ (pH 3) at room temperature at a scan rate of 10 mV s^{-1}. Mott–Schottky plots were measured in an acidic solution (pH 3) at a frequency of 1 kHz in the dark. The potentials measured were converted to reversible hydrogen electrode (RHE) based on the formula [Eq. (3)]:

$$E_{RHE} = E_{Ag/AgCl} + E_{Ag/AgCl\ vs.\ NHE} + 0.059\,pH \quad (3)$$

in which $E_{Ag/AgCl\ vs.\ NHE}$ is the correction factor for Ag/AgCl with respect to the normal hydrogen electrode (NHE), and equals 0.197 V at 20 °C.

Acknowledgements

This work was supported by the 973 Program (Grant 2014CB932104), the National Natural Science Foundation of China (NSFC), Beijing Natural Science Foundation (Grant 2152022), and the Fundamental Research Funds for the Central Universities (YS1406). This work was also partly supported by the Joint Center for Artificial Photosynthesis, a DOE Energy Innovation Hub, supported through the Office of Science of the U.S. Department of Energy under Award Number DE-SC0004993. AFM

data were collected at the Molecular Materials Research Center of the Beckman Institute of the California Institute of Technology.

Keywords: hydrogen peroxide · mixed metal oxide · oxygen reduction · photocatalysis · sustainable chemistry

[1] R. Hage, A. Lienke, *Angew. Chem. Int. Ed.* **2006**, *45*, 206 – 222; *Angew. Chem.* **2006**, *118*, 212 – 229.

[2] a) Y. Yamada, S. Yoshida, T. Honda, S. Fukuzumi, *Energy Environ. Sci.* **2011**, *4*, 2822 – 2825; b) Y. Yamada, M. Yoneda, S. Fukuzumi, *Chem. Eur. J.* **2013**, *19*, 11733 – 11741; c) L. Han, S. J. Guo, P. Wang, S. J. Dong, *Adv. Energy Mater.* **2015**, *5*, 1400424.

[3] J. M. Campos-Martin, G. Blanco-Brieva, J. L. G. Fierro, *Angew. Chem. Int. Ed.* **2006**, *45*, 6962 – 6984; *Angew. Chem.* **2006**, *118*, 7116 – 7139.

[4] a) Y. Yamada, A. Nomura, T. Miyahigashi, S. Fukuzumi, *Chem. Commun.* **2012**, *48*, 8329 – 8331; b) V. Maurino, C. Minero, G. Mariella, E. Pelizzetti, *Chem. Commun.* **2005**, 2627 – 2629; c) T. Hirakawa, Y. Nosaka, *J. Phys. Chem. C* **2008**, *112*, 15818 – 15823.

[5] H. Park, Y. Park, W. Kim, W. Choi, *J. Photochem. Photobiol. C* **2013**, *15*, 1 – 20.

[6] a) D. Tsukamoto, A. Shiro, Y. Shiraishi, Y. Sugano, S. Ichikawa, S. Tanaka, T. Hirai, *ACS Catal.* **2012**, *2*, 599 – 603; b) M. Teranishi, S. Naya, H. Tada, *J. Am. Chem. Soc.* **2010**, *132*, 7850 – 7851; c) H. Sheng, Q. Li, W. H. Ma, H. W. Ji, C. C. Chen, J. C. Zhao, *Appl. Catal. B* **2013**, *138 – 139*, 212 – 218; d) A. H. Michael, *Surf. Sci. Rep.* **2011**, *66*, 185 – 297; e) V. Maurino, C. Minero, G. Mariella, E. Pelizzetti, *Chem. Commun.* **2005**, 2627 – 2629; f) H. Sheng, H. Ji, W. Ma, C. Chen, J. Zhao, *Angew. Chem. Int. Ed.* **2013**, *52*, 9686 – 9690; *Angew. Chem.* **2013**, *125*, 9868 – 9872.

[7] Y. Shiraishi, S. Kanazawa, Y. Sugano, D. Tsukamoto, H. Sakamoto, S. Ichikawa, T. Hirai, *ACS Catal.* **2014**, *4*, 774 – 780.

[8] a) X. C. Wang, S. Blechert, M. Antonietti, *ACS Catal.* **2012**, *2*, 1596 – 1606; b) Y. Wang, X. C. Wang, M. Antonietti, *Angew. Chem. Int. Ed.* **2012**, *51*, 68 – 89; *Angew. Chem.* **2012**, *124*, 70 – 92; c) R. C. Pawar, V. Khare, C. S. Lee, *Dalton Trans.* **2014**, *43*, 12514 – 12527; d) R. C. Pawar, S. Kang, S. H. Ahn, C. S. Lee, *RSC Adv.* **2015**, *5*, 24281 – 24292; e) R. C. Pawar, Y. Pyo, S. H. Ahn, C. S. Lee, *Appl. Catal. B* **2015**, *176 – 177*, 654 – 666; f) Y. Cao, Z. Zhang, J. Long, J. Liang, H. Lin, H. Lin, X. Wang, *J. Mater. Chem. A* **2014**, *2*, 17797 – 17807.

[9] a) H. Zhuang, L. Yang, J. Xu, F. Li, Z. Zhang, H. Lin, J. Long, X. Wang, *Sci. Rep.* **2015**, *5*, 16947; b) J. Xu, L. Luo, G. Xiao, Z. Zhang, H. Lin, X. Wang, J. Long, *ACS Catal.* **2014**, *4*, 3302 – 3306.

[10] a) Y. Shiraishi, S. Kanazawa, Y. Kofuji, H. Sakamoto, S. Ichikawa, S. Tanaka, T. Hirai, *Angew. Chem. Int. Ed.* **2014**, *53*, 13454 – 13459; *Angew. Chem.* **2014**, *126*, 13672 – 13677; b) H. Goto, Y. Hanada, T. Ohno, M. Matsumura, *J. Catal.* **2004**, *225*, 223 – 229; c) R. Cai, Y. Kubota, A. Fujishima, *J. Catal.* **2003**, *219*, 214 – 218; d) Y. Shiraishi, S. Kanazawa, D. Tsukamoto, A. Shiro, Y. Sugano, T. Hirai, *ACS Catal.* **2013**, *3*, 2222 – 2227.

[11] a) G. Moon, W. Kim, A. D. Bokare, N. Sung, W. Choi, *Energy Environ. Sci.* **2014**, *7*, 4023 – 4028; b) S. Kato, J. Jung, T. Suenobu, S. Fukuzumi, *Energy Environ. Sci.* **2013**, *6*, 3756 – 3764; c) N. Kaynan, B. A. Berke, O. Hazut, R. Yerushalmi, *J. Mater. Chem. A* **2014**, *2*, 13822 – 13826.

[12] a) X. Xiang, H. I. Hima, H. Wang, F. Li, *Chem. Mater.* **2008**, *20*, 1173 – 1182; b) X. Xiang, L. S. Xie, Z. W. Li, F. Li, *Chem. Eng. J.* **2013**, *221*, 222 – 229; c) X. Xiang, L. Bai, F. Li, *AIChE J.* **2010**, *56*, 2934 – 2945; d) W. He, Y. Yang, L. Wang, J. Yang, X. Xiang, D. Yan, F. Li, *ChemSusChem* **2015**, *8*, 1568 – 1576; e) W. He, R. Wang, L. Zhang, J. Zhu, X. Xiang, F. Li, *J. Mater. Chem. A* **2015**, *3*, 17977 – 17982.

[13] Z. Q. Huang, J. J. Jiang, Y. M. Hua, C. Z. Li, M. Wagner, H. J. Lewerenz, M. P. Soriaga, C. Anfuso, *Energy Environ. Focus.* **2015**, *4*, 260 – 277.

[14] J. Chen, S. H. Shen, P. H. Guo, P. Wu, L. J. Guo, *J. Mater. Chem. A* **2014**, *2*, 4605 – 4612.

[15] G. Fan, X. Xiang, J. Fan, F. Li, *J. Mater. Chem.* **2010**, *20*, 7378 – 7385.

[16] a) J. Qi, W. Zhang, R. Xiang, K. Liu, H.-Y. Wang, M. Chen, Y. Han, R. Cao, *Adv. Sci.* **2015**, *2*, 1500199; b) G. Natu, P. Hasin, Z. J. Huang, Z. Q. Ji, M. F. He, Y. Y. Wu, *ACS Appl. Mater. Interfaces* **2012**, *4*, 5922 – 5929; c) L. Trotochaud, S. L. Young, J. K. Ranney, S. W. Boettcher, *J. Am. Chem. Soc.* **2014**, *136*, 6744 – 6753.

[17] R. Dedryve're, M. Maccario, L. Croguennec, F. L. Cras, C. Delmas, D. Gonbea, *Chem. Mater.* **2008**, *20*, 7164 – 7170.

[18] Y. Shiraishi, Y. Kofuji, H. Sakamoto, S. Tanaka, S. Ichikawa, T. Hirai, *ACS Catal.* **2015**, *5*, 3058 – 3066.

[19] L.-F. Gao, T. Wen, J.-Y. Xu, X.-P. Zhai, M. Zhao, G.-W. Hu, P. Chen, Q. Wang, H.-L. Zhang, *ACS Appl. Mater. Interfaces* **2016**, *8*, 617 – 624.

[20] B. Li, Y. Zhao, S. Zhang, W. Gao, M. Wei, *ACS Appl. Mater. Interfaces* **2013**, *5*, 10233 – 10239.

[21] a) A. J. Hoffman, E. R. Carraway, M. R. Hoffman, *Environ. Sci. Technol.* **1994**, *28*, 776 – 785; b) C. Kormann, D. W. Bahnemann, M. R. Hoffman, *Environ. Sci. Technol.* **1988**, *22*, 798 – 806.

[22] a) D. Friebel, M. W. Louie, M. Bajdich, K. E. Sanwald, Y. Cai, A. M. Wise, M. J. Cheng, D. Sokaras, T. C. Weng, R. A. Mori, R. C. Davis, J. R. Bargar, J. K. Nørskov, A. Nilsson, A. T. Bell, *J. Am. Chem. Soc.* **2015**, *137*, 1305 – 1313; b) R. D. L. Smith, M. S. Prévot, R. D. Fagan, Z. P. Zhang, P. A. Sedach, M. K. J. Siu, S. Trudel, C. P. Berlinguette, *Science* **2013**, *340*, 60 – 63; c) R. D. L. Smith, M. S. Prévot, R. D. Fagan, S. Trudel, C. P. Berlinguette, *J. Am. Chem. Soc.* **2013**, *135*, 11580 – 11586; d) A. Indra, P. W. Menezes, N. R. Sahraie, A. Bergmann, C. Das, M. Tallarida, D. Schmeißer, P. Strasser, M. Driess, *J. Am. Chem. Soc.* **2014**, *136*, 17530 – 17536.

[23] a) K. Fominykh, P. Chernev, I. Zaharieva, J. Sicklinger, G. Stefanic, A. Döblinger, M. Müller, A. Pokharel, S. Böcklein, C. Scheu, T. Bein, D. F. Rohlfing, *ACS Nano* **2015**, *9*, 5180 – 5188; b) J. Landon, E. Demeter, N. C. Keturakis, I. E. Wachs, R. Vasić, A. I. Frenkel, J. R. Kitchin, *ACS Catal.* **2012**, *2*, 1793 – 1801; c) Y. F. Li, A. Selloni, *ACS Catal.* **2014**, *4*, 1148 – 1153; d) J. A. Bau, E. J. Luber, J. M. Buriak, *ACS Appl. Mater. Interfaces* **2015**, *7*, 19755 – 19763.

[24] S. J. Guo, S. Zhang, L. H. Wu, S. H. Sun, *Angew. Chem. Int. Ed.* **2012**, *51*, 11770 – 11773; *Angew. Chem.* **2012**, *124*, 11940 – 11943.

[25] C. Zhao, H. Luo, F. Chen, P. Zhang, L. Yi, K. You, *Energy Environ. Sci.* **2014**, *7*, 1700 – 1707.

[26] R. L. Spray, K. J. McDonald, K.-S. Choi, *J. Phys. Chem. C* **2011**, *115*, 3497 – 3506.

[27] J. Liu, Y. Liu, N. Liu, Y. Han, X. Zhang, H. Huang, Y. Lifshitz, S.-T. Lee, J. Zhong, Z. Kang, *Science* **2015**, *347*, 970 – 974.

[28] Y. Gong, J. Wang, Z. Wei, P. Zhang, H. Li, Y. Wang, *ChemSusChem* **2014**, *7*, 2303 – 2309.

[29] J. Chen, P. Wagner, L. Tong, G. G. Wallace, D. L. Officer, G. F. Sweigers, *Angew. Chem. Int. Ed.* **2012**, *51*, 1907 – 1910; *Angew. Chem.* **2012**, *124*, 1943 – 1946.

Received: May 26, 2016
Published online on August 3, 2016